Electron Acceleration in Blazars: Application to the 3C 279 Flare on 2013 December 20

Tiffany R. Lewis[1,2] , Justin D. Finke[3] , and Peter A. Becker[4]

[1] Haifa Research Center for Theoretical Physics & Astrophysics, University of Haifa, Mt. Carmel. Haifa 3498838, Israel; tiffanylewisphd@gmail.com
[2] Department of Astrophysics, Faculty of Exact Sciences, Tel Aviv University, P.O. Box 39040, Tel Aviv 6997801, Israel
[3] U.S. Naval Research Laboratory, Code 7653, 4555 Overlook Avenue SW, Washington, DC 20375-5352, USA
[4] Department of Physics & Astronomy, MSN 3F3, George Mason University, 4400 University Drive, Fairfax, VA 22030, USA
Received 2019 July 12; revised 2019 September 8; accepted 2019 September 9; published 2019 October 17

Abstract

The broadband spectrum from the 2013 December 20 γ-ray flare from 3C 279 is analyzed with our previously developed one-zone blazar jet model. We are able to reproduce two spectral energy distributions (SEDs), a quiescent and flaring state, the latter of which had an unusual SED, with hard γ-ray spectrum, high Compton dominance, and short duration. Our model suggests that there is insufficient energy for a comparable X-ray flare to have occurred simultaneously, which is an important constraint given the lack of X-ray data. We show that first- and second-order Fermi acceleration are sufficient to explain the flare, and that magnetic reconnection is not needed. The model includes particle acceleration, escape, and adiabatic and radiative energy losses, including the full Compton cross section, and emission from the synchrotron, synchrotron self-Compton, and external Compton processes. We provide a simple analytic approximation to the electron distribution solution to the transport equation that may be useful for simplified modeling in the future.

Unified Astronomy Thesaurus concepts: Radio-loud quasars (1349); Nonthermal radiation sources (1119); Active galactic nuclei (16); Jets (870); Galaxy jets (601); Blazars (164); Relativistic jets (1390); Radio jets (1347)

1. Introduction

Blazars, the most energetic sustained phenomena in the known universe, are radio-loud active galactic nuclei (AGNs) with relativistic jets closely aligned with our line of sight. The broadband spectral energy distributions (SEDs) from blazars are dominated by beamed jet emission. Blazars are known for their variable broadband spectral features, extending from radio through γ-rays. Their broadband SEDs are characterized by two primary features. In leptonic models, those include a synchrotron peak at lower energies and a Compton peak at higher energies. Alternatively, the high-energy peak can be produced by proton synchrotron (e.g., Aharonian 2000; Mücke et al. 2003; Reimer et al. 2004) or the decay products of proton–photon interactions (e.g., Sikora et al. 1987; Mannheim & Biermann 1992; Protheroe 1995), however hadronic processes are disfavored in some cases due to the excessive energy requirements (e.g., Böttcher et al. 2013; Zdziarski et al. 2015; Petropoulou & Dermer 2016). Blazars are divided into flat-spectrum radio quasars (FSRQs) and BL Lac objects based on their optical spectra, with the former having strong broad emission lines, while the latter do not. FSRQs are thought to have their γ-ray emission dominated by the external Compton (EC) process, where the seed photon fields for Compton scattering come from outside the jet, from sources such as the broad-line region (BLR; e.g., Sikora et al. 1994; Blandford & Levinson 1995; Ghisellini & Madau 1996), dust torus (e.g., Kataoka et al. 1999; Błażejowski et al. 2000), and accretion disk (e.g., Dermer et al. 1992; Dermer & Schlickeiser 1993).

Blazars are characterized by stochastic variability (e.g., Finke & Becker 2014, 2015; Lewis et al. 2016, hereafter Paper I). For example, the FSRQ 3C 279 alternates between quiescence and flaring states over periods of a few days to several weeks (e.g., Hayashida et al. 2012, 2015). Additionally, FSRQs can exhibit isolated flaring activity at optical, X-ray, or γ-ray energies (e.g., Osterman Meyer et al. 2009; Hayashida et al. 2012; MacDonald et al. 2017), or correlated flares

(e.g., Hayashida et al. 2012; Marscher 2012; Liodakis et al. 2018). A single blazar can also exhibit different types of flares at different times (e.g., Hayashida et al. 2012; Vittorini et al. 2014; Kaur & Baliyan 2018, and references therein), and currently there is no consensus on an explanation for why some flares exhibit correlated variability and some do not.

Particle acceleration is a necessity in astrophysical jets in order to explain how the radiating particles reach the energies required to produce the observed emission. However, currently there is no consensus on the precise combination of required acceleration mechanisms, or on their effects on the observed blazar spectra (e.g., Madejski & Sikora 2016; Romero et al. 2017). The first-order Fermi process, resulting from acceleration at a shock front, is widely assumed to contribute to particle acceleration in blazars (e.g., Bednarek & Protheroe 1997; Tavecchio et al. 1998; Bednarek & Protheroe 1999; Finke et al. 2008; Dermer et al. 2009; Hayashida et al. 2012). On its own, first-order Fermi acceleration produces a power-law particle spectrum (Fermi 1949). This can be attenuated by radiative loss mechanisms, especially synchrotron, which impose an exponential cutoff at high energies. Second-order Fermi (stochastic) acceleration is also thought to contribute to electron energization in blazars (e.g., Summerlin & Baring 2012; Baring et al. 2017). Stochastic acceleration alone gives a log-parabola electron distribution (ED) (e.g., Tramacere et al. 2011).

We previously developed a steady-state model for particle acceleration and emission in blazar jets which included first- and second-order Fermi acceleration of particles, and radiation by synchrotron, synchrotron self-Compton (SSC), and EC mechanisms (Lewis et al. 2018, hereafter Paper II). EC of photons from a realistic, stratified BLR (Finke 2016) and dust torus were included. Here we exercise this model in a new situation: modeling the extreme flare from 3C 279 observed on 2013 December 20.

The familiar blazar 3C 279 has been very well observed at all wavelengths for many years (e.g., Grandi et al. 1996;

Wehrle et al. 1998; Chatterjee et al. 2008; Hayashida et al. 2012). On 2013 December 20, the source was observed by the *Fermi* Large Area Telescope (LAT) to have a flare that was extremely hard in γ rays (photon spectral index $\Gamma_\gamma \sim 1.7$, compared to 2.4 right before the flare), with the peak of the γ-ray emission shifting from below the *Fermi*-LAT energy range ($h\nu^{\rm peak} \lesssim 100\,{\rm MeV}$) immediately before the flare, to over a decade in energy higher, $h\nu^{\rm peak} \gtrsim 2\,{\rm GeV}$ (Hayashida et al. 2015). At the same time, the peak of the synchrotron spectrum stayed nearly constant, and may have even shifted to slightly higher frequencies; the Compton dominance was estimated to be an extreme $A_{\rm C} = L_\gamma/L_{\rm syn} \gtrsim 300$. The flux-doubling timescale was rapid, $\approx 2\,{\rm hr}$, although still less extreme than the minute-scale variability found by Ackermann et al. (2016) for the 2015 June flare from 3C 279.

The 2013 December 20 flare has attracted some attention from modelers due to its unusual properties (e.g., Asano & Hayashida 2015; Hayashida et al. 2015; Paliya et al. 2016), although no firm conclusions regarding the particle acceleration mechanism have been drawn. Here we apply our steady-state blazar acceleration and emission model to this problem.

The paper is organized as follows. In Section 2, we give a brief summary of our jet model, which includes a steady-state, self-consistent electron transport equation (including first- and second-order Fermi acceleration; synchrotron and Compton losses). In Section 3, we apply the model to the extreme 2013 December 20 γ-ray flare of 3C 279 (as well as the preceding quiescent period) to obtain new physical insights. We discuss and interpret the results of the analysis in Section 4. We include a derivation of the simplified analytic ED in Appendix A. In Appendix B, we provide derivations related to the physical interpretation of the ED shape.

2. Model

The blazar jet originates from a supermassive black hole (BH), perhaps accelerated by a rapidly spinning BH threaded with magnetic fields anchored in an accretion disk (Blandford & Znajek 1977). The jet plasma moves outward from the BH, and toward the observer, with some bulk Lorentz factor $\Gamma = (1 - \beta^2)^{-1/2}$, which is related to the relativistic bulk speed $v = \beta c$, where c is the speed of light. The material moves relativistically toward the observer, within some small angle θ to the line of sight, leading to a Doppler factor $\delta_{\rm D} = [\Gamma(1 - \beta \cos \theta)]^{-1}$. We assume $\delta_{\rm D} = \Gamma$.

The primary emitting region is modeled as a single, compact homogeneous zone or "blob." The co-moving blob is causally connected by the light-crossing timescale, $t_{\rm var}$, which is the minimum variability timescale in the observer's frame. Thus, the radius of the blob (in the frame co-moving with the jet) must be $R_b' \lesssim c\delta_{\rm D} t_{\rm var}/(1 + z)$, where z denotes the cosmological redshift of the source. Radio emission is produced throughout the jet via synchrotron emission (e.g., Blandford & Königl 1979; Königl 1981; Finke 2019). The relatively small size of the blob radius implied by the observed variability timescales suggests that significant synchrotron self-absorption occurs in the blob, making it unlikely that the blob is the source of the observed radio emission. The radio emission thus provides upper limits on the emission from the region considered here.

2.1. Electron Energy Distribution

Throughout the data comparison process, we use the numerical model, including the self-consistent ED (Paper II). We describe the ED $N_e(\gamma)$ in the frame of the blob using a steady-state Fokker–Planck equation,

$$0 = \frac{\partial^2}{\partial \gamma^2}\left(\frac{1}{2}\frac{d\sigma^2}{dt}N_e\right) - \frac{\partial}{\partial \gamma}\left(\left\langle \frac{d\gamma}{dt} \right\rangle N_e\right)$$
$$- \frac{N_e}{t_{\rm esc}} + \dot{N}_{\rm inj}\delta(\gamma - \gamma_{\rm inj}), \tag{1}$$

where $\gamma \equiv E/(m_e c^2)$ is the electron Lorentz factor, m_e is the electron mass, and c is the speed of light in a vacuum. Since this is a steady-state equation, we have set $\partial N_e/\partial t = 0$. The acceleration and synchrotron energy loss timescales are appreciably shorter than the observed rise time of the flare (see Section 3.5), making the steady-state calculation appropriate in this case. We note that we use the term "electrons" here and throughout this paper to refer to both electrons and positrons.

In Equation (1), the energy-dependent particle escape timescale, $t_{\rm esc}$, is related to the dimensionless escape parameter τ via

$$t_{\rm esc}(\gamma) = \frac{\tau}{D_0 \gamma}, \tag{2}$$

where

$$\tau \equiv \frac{R_b'^2 q B D_0}{m_e c^3}, \tag{3}$$

in the Bohm limit (Paper I), and q is the fundamental charge. The Lorentz factor of the injected electrons is $\gamma_{\rm inj}$ in the particle injection rate

$$\dot{N}_{\rm inj} = \frac{L_{\rm e,inj}}{m_e c^2 \gamma_{\rm inj}}, \tag{4}$$

where $L_{\rm e,inj}$ is the electron injection luminosity. Both $\gamma_{\rm inj}$ and $L_{\rm e,inj}$ are implemented as free parameters, but the former is held constant in the subsequent analysis at the lower numerical grid limit to simulate a thermal particle source. We solved Equation (1) using the full Compton energy loss rate numerically, as described in Paper II.

In Equation (1), the broadening coefficient

$$\frac{1}{2}\frac{d\sigma^2}{dt} = D_0 \gamma^2, \tag{5}$$

is consistent with hard-sphere scattering, where $D_0 \propto {\rm s}^{-1}$ (Park & Petrosian 1995) is a free parameter. The drift coefficient expresses the mean rate at which each process contributes

$$\left\langle \frac{d\gamma}{dt} \right\rangle = D_0\left[4\gamma + a\gamma - b_{\rm syn}\gamma^2 - \gamma^2\sum_{j=1}^{J}b_{\rm C}^{(j)}H(\gamma\epsilon_{\rm ph}^{(j)})\right], \tag{6}$$

where second-order Fermi acceleration occurs at a rate of

$$\dot{\gamma}_{\rm sto} = 4D_0\gamma, \tag{7}$$

and

$$\dot{\gamma}_{\rm ad+sh} \equiv aD_0\gamma \equiv A_{\rm ad+sh}\gamma, \tag{8}$$

where a is a dimensionless free parameter that includes first-order Fermi acceleration and adiabatic cooling.[5] The coefficients $A_{\rm sh}$ and $A_{\rm ad}$ represent the first-order Fermi acceleration rate and the adiabatic loss rate, respectively. The rate of synchrotron cooling is

$$|\dot{\gamma}_{\rm syn}| \equiv D_0 b_{\rm syn} \gamma^2 = \frac{\sigma_{\rm T} B^2}{6\pi m_e c}\gamma^2, \qquad (9)$$

where $\sigma_{\rm T} = 6.65 \times 10^{-25}\,{\rm cm}^2$ is the Thomson cross section and B is the strength of the tangled, homogeneous magnetic field. Similarly, the Compton cooling rate for each individual component is

$$|\dot{\gamma}_{\rm C}| \equiv D_0 \gamma^2 b_{\rm C}^{(j)} H(\gamma \epsilon_{\rm ph}^{(j)}) \equiv \gamma^2 B_{\rm C}^{(j)} H(\gamma \epsilon_{\rm ph}^{(j)})$$
$$= \gamma^2 \frac{4\sigma_{\rm T}\Gamma^2 u_{\rm ph}^{(j)}}{3 m_e c} H(\gamma \epsilon_{\rm ph}^{(j)}). \qquad (10)$$

Here $b_{\rm C}^{(j)}$ is a dimensionless constant related to Compton cooling for the different external radiation fields j, with energy densities $u_{\rm ph}^{(j)}$. The function $H(y)$ is a complicated expression related to mitigation of energy losses with the full Compton cross section (Böttcher et al. 1997). We include a dust torus and 26 broad lines, for a total of $J = 27$ EC components (Finke 2016).

2.2. Thomson Regime Approximation

In the Thomson limit, $y \ll 1$, $H(y) \to 1$, the steady-state Fokker–Planck equation (Equation (1)) has the analytic solution (see Paper I for details)

$$N_e(\gamma) = \frac{\dot{N}_{\rm inj}}{b D_0}\frac{\Gamma(\mu - \kappa + 1/2)}{\Gamma(1+2\mu)}e^{(\gamma_{\rm inj}-\gamma)b/2}\gamma_{\rm inj}^{-2-a/2}\gamma^{a/2}$$
$$\times \begin{cases} \mathcal{M}_{\kappa,\mu}(b\gamma)\mathcal{W}_{\kappa,\mu}(b\gamma_{\rm inj}), & \gamma \leqslant \gamma_{\rm inj} \\ \mathcal{M}_{\kappa,\mu}(b\gamma_{\rm inj})\mathcal{W}_{\kappa,\mu}(b\gamma), & \gamma_{\rm inj} \leqslant \gamma \end{cases}, \qquad (11)$$

where $b \equiv b_{\rm syn} + \sum_{j=1}^{J} b_{\rm C}^{(j)}$, $\mathcal{M}_{\kappa,\mu}$ and $\mathcal{W}_{\kappa,\mu}$ are Whittaker functions (Slater 1960), with coefficients

$$\kappa = 2 - \frac{1}{b\tau} + \frac{a}{2}, \quad \text{and} \quad \mu = \frac{a+3}{2}. \qquad (12)$$

We found the analytic Thomson regime solution, Equation (11), previously (Paper I). Here we provide a useful approximation,

$$N_e^{\rm app}(\gamma) \approx \frac{\dot{N}_{\rm inj}}{D_0}e^{-b\gamma}\left[\frac{\tau b^{a+4}\gamma^{a+2}}{\Gamma(a+4)} + \frac{1}{3+a}\frac{1}{\gamma}\right], \qquad (13)$$

in the $\gamma_{\rm inj} < \gamma$ regime (where most of our analysis takes place), and where $b\gamma \ll 1$ and $(b\tau)^{-1} \ll 1$ are the simplifying assumptions, which are valid in all blazar analyses we have examined, both here and in Paper II. The precision of these assumptions is addressed further in Appendix A, however the simplified solution is relatively accurate for most applications, except where $(b\tau)^{-1} \gtrsim 1$.

The constraint $b\gamma \ll 1$ indicates that the rate of particle energy lost to synchrotron (Equation (9)) and Thomson processes
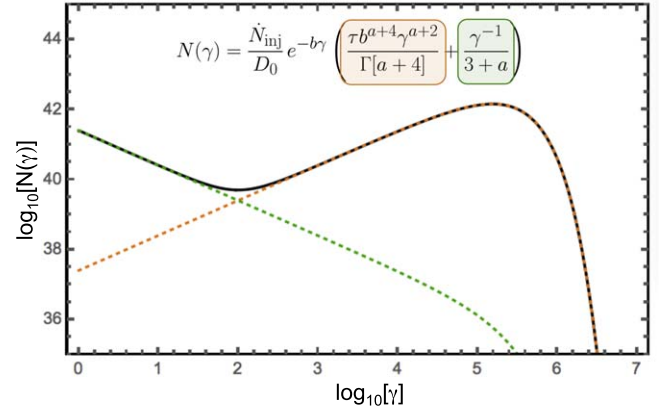
Figure 1. This sample ED uses contrived parameters to showcase the two components from the $\gamma \geqslant \gamma_{\rm inj}$ branch of Equation (13). The orange line is given by a balance between the the first-order Fermi/adiabatic and second-order acceleration terms (Appendix B), and $a > -2$, giving a positive power law, and an excess of high-energy particles. The green line is dominated by second-order Fermi (stochastic) acceleration of particles to higher energies (Appendix B). Both terms are independently affected by the exponential cutoff due to emission mechanisms. The black line is the full Thomson regime solution (Equation (11)).

(Equation (10), for $H(\epsilon\gamma) = 1$), where $(b = b_{\rm syn} + b_{\rm C}^{(j)})$ must be smaller than the rate at which energy is gained by the second-order Fermi process (Equation (7)). Thus, the emitting blob must be in the acceleration region, which can be demonstrated by the energy budget for the flare presented in this work (Section 3.4). Similarly, the requirement $(b\tau)^{-1} \ll 1$ is analogous to the expectation that the energy losses due to the synchrotron and Thomson processes outpace energy lost due to particle escape (i.e., the fast-cooling regime), which is apparent in the present application by examining the energy budget (Section 3.4).

The full derivation and complementing solution for $\gamma > \gamma_{\rm inj}$ are given in Appendix A. The main shape of the ED is governed by two components: one is driven by a balance between first- and second-order Fermi acceleration ($\propto \gamma^{a+2}$; orange curve in Figure 1) and the other is due to second-order Fermi acceleration ($\propto \gamma^{-1}$; green curve in Figure 1; see Appendix B). The ratio of first- to second-order Fermi acceleration acceleration (parameterized by $a = A_{\rm ad+sh}/D_0$) impacts the shared term. When $a < -2$, the lower energy power law is negative, and when $a > -2$, the $\propto \gamma^{a+2}$ term is increasing with increasing energy. In practice, the shape of the the term does not vary significantly for most analyses, but is important in simulating the flare examined here. The exponential cutoff is governed by the emission mechanisms, which are constrained to the Thomson limit for the analytic solution. Appendix A discusses the interpretation of the acceleration mechanisms in the simplified solution in further detail.

The analytic solution and others derived from it, are useful for physical interpretation of the shape of the ED with regard to acceleration mechanisms. However, all of the data interpretation here is performed with the full numerical model using the full Compton cross section and energy losses.

2.3. Spectral Emission Processes

We include thermal emission from the accretion disk (Shakura & Sunyaev 1973) and dust torus, in addition to emission from the jet from synchrotron, SSC, and EC of dust

---

[5] For $a > 0$ first-order Fermi acceleration dominates over adiabatic losses; for $a < 0$, the opposite is true.

torus and BLR photons. The source 3C 279 has redshift $z = 0.536$, giving it a luminosity distance $d_L = 9.6 \times 10^{27}$ cm in a cosmology where $(h, \Omega_m, \Omega_\Lambda) = (0.7, 0.3, 0.7)$.

The νF_ν disk flux is approximated as

$$f_{\epsilon_{obs}}^{disk} = \frac{1.12}{4\pi d_L^2}\left(\frac{\epsilon}{\epsilon_{max}}\right)^{4/3} e^{-\epsilon/\epsilon_{max}}, \qquad (14)$$

(Dermer et al. 2014), where $\epsilon = \epsilon_{obs}(1 + z)$ and $m_e c^2 \epsilon_{max} = 10$ eV. The νF_ν dust torus flux is approximated as a blackbody,

$$f_{\epsilon_{obs}}^{dust} = \frac{15 L^{dust}}{4\pi^5 d_L^2} \frac{(\epsilon/\Theta)^4}{\exp(\epsilon/\Theta) - 1}, \qquad (15)$$

where again $\epsilon = \epsilon_{obs}(1 + z)$, and also $\Theta = k_B T_{dust}/(m_e c^2)$, T_{dust} is the dust temperature, and k_B is the Boltzmann constant.

The jet blob νF_ν flux is computed using the ED solution to the electron Fokker–Planck equation (Equation (1)), $N_e'(\gamma')$. We now add primes to indicate the distribution is in the frame co-moving with the jet blob.

The synchrotron flux

$$f_{\epsilon_{obs}}^{syn} = \frac{\sqrt{3}\,\epsilon'\delta_D^4 e^3 B}{4\pi h d_L^2} \int_1^\infty d\gamma' N_e'(\gamma')\, R(x), \qquad (16)$$

where

$$x = \frac{4\pi\epsilon' m_e^2 c^3}{3eBh\gamma'^2}, \qquad (17)$$

and $R(x)$ is defined by Crusius & Schlickeiser (1986). Synchrotron self-absorption is also included. The SSC flux

$$f_{\epsilon_s}^{SSC} = \frac{9}{16}\frac{(1 + z)^2 \sigma_T \epsilon_s'^2}{\pi\delta_D^2 c^2 t_v^2}\int_0^\infty d\epsilon_*'\, \frac{f_{\epsilon_*}^{syn}}{\epsilon_*'^3}$$
$$\times \int_{\gamma_1'}^\infty d\gamma'\frac{N_e'(\gamma')}{\gamma'^2} F_C\left(4\gamma'\epsilon_*', \frac{\epsilon}{\gamma'}\right), \qquad (18)$$

(e.g., Finke et al. 2008), where $\epsilon_s' = \epsilon_s(1 + z)/\delta_D$, $\epsilon_*' = \epsilon_*(1 + z)/\delta_D$, and

$$\gamma_1' = \frac{1}{2}\epsilon_s'\left(1 + \sqrt{1 + \frac{1}{\epsilon'\epsilon_s'}}\right). \qquad (19)$$

The function $F_C(p, q)$ was originally derived by Jones (1968), but had a mistake that was corrected by Blumenthal & Gould (1970). The EC flux (e.g., Georganopoulos et al. 2001; Dermer et al. 2009)

$$f_{\epsilon_s}^{EC} = \frac{3}{4}\frac{c\sigma_T \epsilon_s^2}{4\pi d_L^2}\frac{u_*}{\epsilon_*^2}\delta_D^3$$
$$\times \int_{\gamma_1}^{\gamma_{max}} d\gamma\frac{N_e'(\gamma/\delta_D)}{\gamma^2} F_C\left(4\gamma\epsilon_*, \frac{\epsilon_s}{\gamma}\right), \qquad (20)$$

where

$$\gamma_1 = \frac{1}{2}\epsilon_s\left(1 + \sqrt{1 + \frac{1}{\epsilon\epsilon_s}}\right), \qquad (21)$$

and u_* and ϵ_* are the energy density and dimensionless photon energy of the external radiation field, respectively. For the dust

Table 1
Free Model Parameters

Parameter (Unit)	Model A	Model B1	Model B2	Model B3
t_{var} (s)	1.5×10^4	3.5×10^4	2.3×10^3	9.0×10^2
B (G)	1.3	0.07	0.21	0.3
δ_D	30	18	49	70
r_{blob} (cm)	1.9×10^{17}	1.4×10^{17}	1.6×10^{17}	1.3×10^{17}
ξ_{dust}[a]	0.1	0.1	0.1	0.1
T_{dust}[a] (K)	1470	1470	1470	1470
L_{disk}[a] (erg s^{-1})	1.0×10^{45}	1.0×10^{45}	1.0×10^{45}	1.0×10^{45}
D_0 (s^{-1})	7.0×10^{-6}	2.5×10^{-6}	9.0×10^{-6}	1.5×10^{-5}
a	-4.1	$+1.0$	-2.0	-0.5
γ_{inj}[b]	1.01	1.01	1.01	2.01[b]
L_{inj} (erg s^{-1})	8.8×10^{28}	1.0×10^{32}	8.5×10^{30}	5.4×10^{30}

Notes.
[a] Parameter held constant during analysis, although implemented as free.
[b] The positive slope in the ED at $\gamma \lesssim 10$ confounds the numerical normalization scheme, but the results are essentially equivalent to a Model B3 with $\gamma_{inj} = 1.01$ due to low particle injection number.

torus photons,

$$u_* = u_{dust} = 2.2 \times 10^{-5}\left(\frac{\xi_{dust}}{0.1}\right)\left(\frac{T_{dust}}{1000K}\right)^{5.2}\, erg\, cm^{-3}, \quad (22)$$

and

$$\epsilon_* = \epsilon_{dust} = 5 \times 10^{-7}\left(\frac{T_{dust}}{1000\, K}\right), \qquad (23)$$

consistent with Nenkova et al. (2008). Here ξ_{dust} is a free parameter indicating the fraction of disk photons that are reprocessed by the dust torus. For the BLR photons,

$$u_* = u_{line} = \frac{u_{line,0}}{1 + (r_{blob}/r_{line})^\beta}, \qquad (24)$$

where $\beta \approx 7.7$ (Finke 2016), r_{blob} is the distance of the emitting blob from the BH (a free parameter). The line radii r_{line} and initial energy densities $u_{line,0}$ for all broad lines used are given by the Appendix of Finke (2016) relative to the Hβ line based on the composite Sloan Digital Sky Survey (SDSS) quasar spectrum of Vanden Berk et al. (2001). The parameters r_{line} and $u_{line,0}$ are determined from the disk luminosity using relations found from reverberation mapping, as described by Finke (2016) and in Paper II.

2.4. High-energy Attenuation

Since the analysis of the 2013 December 20 flare predicts very high-energy γ-rays, which could be attenuated, we include $\gamma\gamma$-absorption from the dust torus and BLR photons following Finke (2016). Absorption attenuates the emerging jet emission by a factor $\exp[-\tau_{\gamma\gamma}(\epsilon_1)]$, where $\tau_{\gamma\gamma}(\epsilon_1)$ is the absorption optical depth and ϵ_1 is the dimensionless energy of the higher energy photon produced in the jet. We have computed the Doppler factor where $\gamma\gamma$ absorption with internal synchrotron photons becomes important (e.g., Dondi & Ghisellini 1995; Finke et al. 2008) and found that the minimum Doppler factor is much lower than the value used in our models here (Table 1). Therefore, we hereafter neglect internal synchrotron photoabsorption.

Emission from the BLR comes from a relatively narrow region at sub-parsec scales from the BH and different lines are
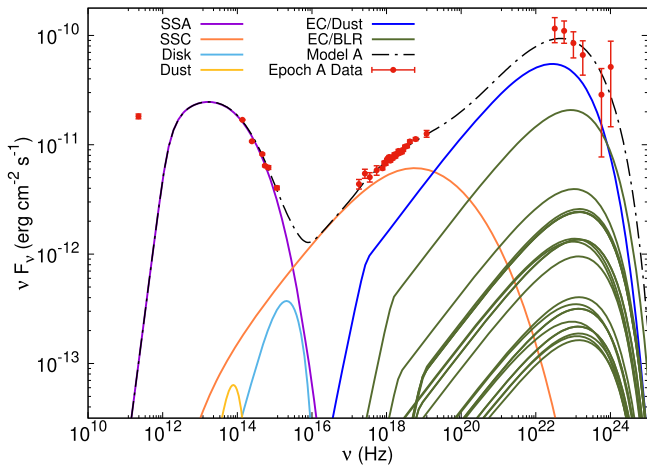
Figure 2. SED of 3C 279 during Epoch A (2013 December 16–19; Hayashida et al. 2015) and our model results. Curves are labeled in the legend.

Figure 3. SED of 3C 279 during Epoch B (2013 December 20; Hayashida et al. 2015) and our three model results (Models B1, B2, and B3). Curves are labeled in the legend. The data and model for Epoch A are also shown in light gray for reference.

produced at different radii (e.g., Peterson & Wandel 1999; Kollatschny 2003; Peterson et al. 2014), which can consist of concentric, infinitesimally thin, spherical shells for each emission line or concentric, infinitesimally thin rings Similarly, the dust torus can be modeled as a ring with an infinitesimally thin annulus or a more extended flattened disk with defined inner and outer radii. After testing each geometry, we find that in all cases $\gamma\gamma$-absorption is unimportant to model the energy range studied here, although attenuation by dust torus photons can have some effect at $\gtrsim 800$ GeV. The following analysis utilizes the concentric shell BLR and ring dust torus geometries, which are consistent with the emission calculations.

3. Application to 3C 279: 2013 December Flare and Preceding Quiescent Period

The 3 days immediately preceding the extreme, Compton-dominant flare of the FSRQ, 3C 279, were quiescent and apparently unremarkable for the source. This period, dubbed "Epoch A" in Hayashida et al. (2015), where the data were originally published occurred on 2013 December 16–19, and is analyzed to look for any unusual parameter values and to provide context for the flare analysis. The isolated γ-ray flare occurred during a 12 hr period on 2013 December 20, dubbed "Epoch B" by Hayashida et al. (2015). In both Epochs A and B, besides the γ-ray data from *Fermi*-LAT, optical and IR data were collected by the Kanata Telescope and the Small and Medium Aperture Research Telescopes (SMARTS). During Epoch A, radio observations were made by the Submillimeter Array (SMA), UV and optical data were collected by *Swift*'s Ultraviolet and Optical Telescope (UVOT), and X-ray data were collected by both *NuSTAR* and *Swift*-XRT. Due to the unexpected nature and short duration of the flare (Epoch B), there were no radio or X-ray observations during that time. We analyzed these SEDs using the model described in Section 2 with the full Compton expressions for radiative cooling and emission, and the numerical solution to the Fokker–Planck equation.

3.1. Particle Acceleration and Spectral Emission

We first analyzed Epoch A with our model. The νF_ν SED data for Epoch A is shown in Figure 2 with our model result,
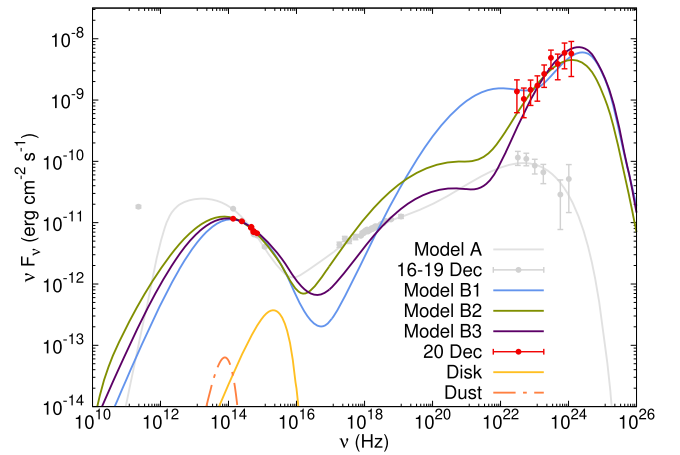
and our model parameters are in Table 1. Figure 2 demonstrates that the γ-ray data is described by a 27 component EC model, including the dust torus and a stratified BLR. Scattering of dust torus photons is the largest single contributor to the production of γ-ray emission, although the sum of all BLR photon scattering is similar. The X-ray data are predominantly reproduced by the SSC process although EC/dust contributes heavily at harder energies. The IR-UV data is reproduced primarily by synchrotron radiation, which includes self-absorption at lower energies. Note that the radio emission is produced outside of the modeled region, so that the data are upper limits on the model.

Figure 3 shows spectral data for Epoch B, which was observed during a 12 hr period on 2013 December 20, immediately following Epoch A. There are no X-ray data available during the 12 hr of peak flare for Epoch B, on 2013 December 20, and as shown in the analysis of Epoch A (Figure 2), the X-rays constrain primarily the SSC component of the spectrum. Thus, the variability timescale t_{var} and Doppler beaming factor δ_D are not well constrained for this epoch. However, since the ED informs the SED and the parameters for the SED emission are all included in the ED as loss parameters, none of the jet components in the spectral model are fully independent from one another. We explore the parameter space with three models, each making different predictions for X-ray emission. Our model parameters for each one are in Table 1. Model B1 is the only one to reproduce the "ankle" in the γ-ray spectrum (i.e., the change in spectral index around 300 MeV), but requires a high SSC flux not previously observed for this source, leading to a very hard X-ray spectrum. For all of the Epoch B models, the γ-ray emission is dominated by scattering of BLR photons (unlike our model for Epoch A, where it was dominated by the scattering of dust photons). Model B2 is an intermediate possibility and predicts a more moderate X-ray spectrum. Model B3 has both the lowest flux and the lowest frequency peak for the SSC. Model B3 also has the smallest timescale for particle acceleration (Section 3.5), which is important since the flux-doubling timescale for the flare was quite short (~ 2 hr). Model B3 has a high Doppler factor, indicating a very high blob velocity. All of the models for Epoch B have different δ_D (and therefore Γ) from the Epoch A model. However, this is not a problem, as the emission in

Table 2
Calculated Parameters

| Parameter (Unit)	Model A	Model B1	Model B2	Model B3
$R_{\mathrm{Ly}\alpha}$ (cm)	2.7×10^{16}	2.7×10^{16}	2.7×10^{16}	2.7×10^{16}
$R_{\mathrm{H}\beta}$ (cm)	1.0×10^{17}	1.0×10^{17}	1.0×10^{17}	1.0×10^{17}
R_b' (cm)	8.5×10^{15}	1.2×10^{16}	2.4×10^{15}	1.2×10^{15}
$\phi_{j,\mathrm{min}}$ (°)	1.3	2.4	0.4	0.5
P_B (erg s^{-1})	8.2×10^{44}	1.6×10^{42}	4.5×10^{42}	5.0×10^{42}
P_e (erg s^{-1})	8.6×10^{45}	2.2×10^{46}	9.0×10^{45}	4.3×10^{45}
ζ_e [a]	1.0×10^{1}	1.4×10^{4}	2.0×10^{3}	8.5×10^{2}
μ_a [b]	3.8	8.8	3.6	1.7
u_{ext} (erg cm^{-3})	3.5×10^{-4}	9.6×10^{-4}	5.8×10^{-4}	1.3×10^{-3}
u_{dust} (erg cm^{-3})	1.6×10^{-4}	1.6×10^{-4}	1.6×10^{-4}	1.6×10^{-4}
u_{BLR} (erg cm^{-3})	1.9×10^{-4}	8.0×10^{-4}	4.2×10^{-4}	1.1×10^{-3}
A_C	4.7	1600	800	1800
L_{jet} (erg s^{-1})	5.0×10^{44}	5.4×10^{46}	4.5×10^{45}	3.1×10^{45}
σ_{max}	4.3	2.9	2.2	1.8

Notes.
[a] $\zeta_e = u_e/u_B = P_e/P_B$ is the equipartition parameter, where $\zeta_e = 1$ indicates equipartition.
[b] $\mu_a \equiv (P_B + P_e)/P_a$ is the ratio of jet to accretion power. Magnetically arrested accretion explains values of $\mu_a \lesssim$ a few.

Epochs A and B are likely produced by different blobs, which can be moving with different Γ, since within a few days for the observer, the distance of a given emitting blob from the BH r_{blob} will change significantly. In Figure 3 the results of the Epoch A analysis are also shown for reference, demonstrating both the difference in the observed γ-ray spectra, as well as the possible changes to the X-rays. All of the B models have harder X-ray spectra for the flare than was observed during the quiescent period, which is qualitatively consistent with the optical and γ-ray hardness changes. Hayashida et al. (2015) estimate the Compton dominance $A_C \geqslant 300$ for Epoch B, and thus classify the flare as a rare, extreme Compton flare. We predict Compton dominance values up to $A_C = 1800$ for Model B3 (Table 2).

Throughout the simulations, we hold constant several parameters that the model can in principle vary (see Table 1). The parameters L_{disk}, ξ_{dust}, and T_{dust} are not expected to vary significantly on timescales of days. The Lorentz factor of particles injected into the base of the blob γ_{inj} is generally taken to be near unity as these particles are expected to originate from the thermal population in the accretion disk. However the numerical machinery can produce incomplete solutions for positive ED slopes near γ_{inj} when $\gamma_{\mathrm{inj}}/\gamma_{\mathrm{max}}$ is very small (and for negative ED slopes near γ_{inj} as $\gamma_{\mathrm{inj}}/\gamma_{\mathrm{max}}$ goes to 1). Thus, for Model B3, we used $\gamma_{\mathrm{inj}} = 2$. However, since the number of particles injected into the blob is low compared to the total number of particles in the ED at the injection energy, the ED solution is effectively the same.

Models A, B2, and B3 have stronger second-order Fermi acceleration (as indicated by a larger D_0), while in Model B1 a first-order Fermi process dominates over adiabatic cooling ($A_{\mathrm{ad+sh}} > 0$). Notably, all of the models are able to represent the available broadband multiwavelength data, suggesting that it is possible for Fermi acceleration processes to meet the acceleration requirements for the observed emission.
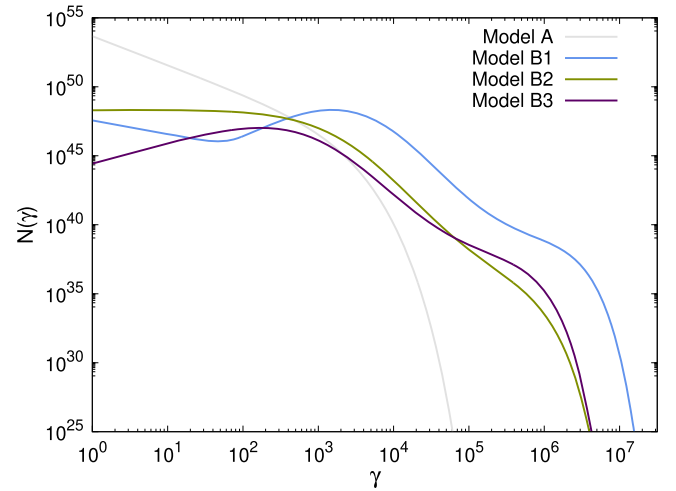
Figure 4. Numerical EDs for the model SEDs in Figure 3. Models B2 and B3 have more particles at higher energies than Model A. Similarly, Model B1 has the most particles occupying the highest energies.

In Figure 3, the data suggest that the peak luminosity of the synchrotron emission decreases during the flare, which might indicate a decrease in the magnetic field B for a similar particle distribution. In Model B1, this effect is exaggerated, with the particle distribution being much more energetic than in Model A, and thus the magnetic field strength is especially low (see Table 1).

The dust and BLR energy densities (u_{dust} and u_{BLR}, respectively) represent the energy in the incident photon fields in the AGN rest frame, and that are available for EC scattering. The combined BLR energy density is elevated by a factor of a few in Model B1 from the Model A values, which are within the previously observed range. The elevated energy density of EC photon sources should be expected of an orphaned γ-ray flare for a similar ED, since the Compton dominance A_C is high (see Table 2). However, in the case of Model B1, the requisite external energy densities are lower because more of the scattering energy is provided by the elevated energy in the ED. Thus Model B1 has more moderate energy requirements from the environment outside the jet than Models B2 and B3.

Models B2 and B3 employ more moderate estimates of the SSC flux, and the magnitude and spectral index in the X-rays are closer to those observed during Epoch A (Figure 3). In both Models B2 and B3, the magnetic field $B \lesssim 0.3\,\mathrm{G}$ (Table 1), is consistent with the analysis in Hayashida et al. (2015). These higher (than Model B1) values for the magnetic field strength produce similar synchrotron simulations because in Models B2 and B3, there is less energy in the jet electrons (Figure 4) and a lower δ_{D}. Additionally, the lower energy ED requires higher δ_{D} and higher energy densities of the external radiation fields due to dust and the BLR to maintain the Compton dominance in the EC portion of the simulation.

3.2. The Particle Distribution

Since the ED for each SED is produced independently from the others, and is an integral part of the simulation, it is instructive to look at the shapes produced for each model. Figure 4 has ED curves for each SED model in Figure 3, with the same color scheme. Model A (gray) appears as a relatively simple power law with an exponential cutoff, which is due to the balance between first-order Fermi (including adiabatic
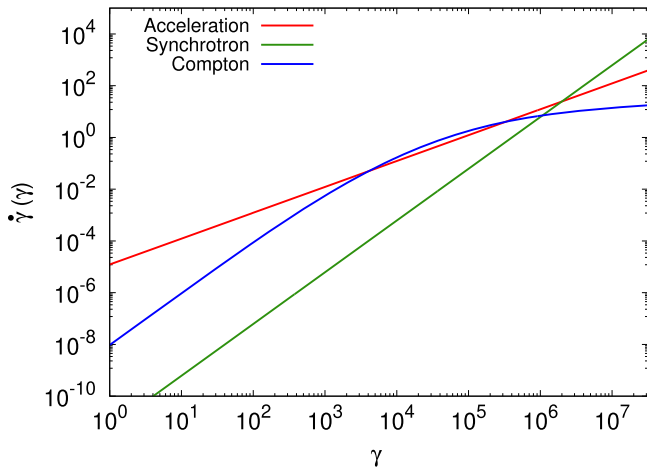
Figure 5. Electron acceleration rate and synchrotron and Compton scattering radiative loss rates in the co-moving frame for Model B1.

expansion) and second-order Fermi accelerations, where the ratio between the two $a = -4.1 < a_{critical} = -2$, thus $N(\gamma)$ is decreasing with increasing γ. The second-order Fermi acceleration dominated portion of the solution is subdominant in Epoch A (acceleration dependencies in the ED are derived in Appendix B).

In each of the Epoch B model EDs, both terms from Equation (13) are apparent, but they are arranged differently in Figure 4 than in Figure 1. The second-order Fermi term, which was cut off around $\gamma_{max} \sim 10^5$ in Figure 1 is cut off at $\gamma_{max} \sim 10^7$ for Model B1 and $\gamma_{max} \sim 10^{6.5}$ for Models B2 and B3 (Figure 4). It is interesting to note that for Model B1, the second-order Fermi component dominates at $10^2 \lesssim \gamma \lesssim 10^5$. All of the cutoffs occur at much higher Lorentz factors than Model A, indicating that acceleration is providing more energy to the particles. So, regardless of the particular simulation, the flare requires more high-energy particles than does the preceding quiescent period. The feature in the EDs at $\gamma \approx 10^{3.5}$ is due to the first-order Fermi/adiabatic/second-order Fermi term in Equation (13). Model B2 has $a = -2$, which produces a slope of 0 in that term. Models B1 and B3 have $a > -2$, and produce positive slopes at $\gamma \lesssim 10^{3.5}$ in the balanced term. Positive slopes indicate that acceleration outpaces emission in that energy range. However, the combined term acceleration is damped by emission mechanisms at much lower energies than the second-order Fermi dominated term for all three Epoch B models.

The approximation Equation (13) is based on the analytic derivation in the Thomson limit. In the numerical solution, we include the full Compton cross section, and it is possible to separate the loss mechanisms. Figure 5 shows the rate of energy gain and loss at each Lorentz factor for Model B1. The red acceleration curve in Figure 5 is given by the sum of acceleration rates for first- and second-order Fermi processes (Equations (8) and (7), respectively). Acceleration dominates at Lorentz factors $\gamma \lesssim 10^{3.5}$, where it is intersected by the blue Compton curve, which corresponds to the first turnover in the ED (Figure 4). The Compton loss rate (Equation (10)) changes at higher energies due to the Klein–Nishina effect, which allows it to trace the acceleration rate through $\gamma \sim 10^5$, causing a decline in the ED over the same range (Figure 4). The synchrotron loss rate (Equation (9)) is subdominant until

$\gamma \gtrsim 10^6$, at which point it provides the definitive exponential cutoff to the ED.

3.3. Jet Dynamics and Geometry

Our model gives $r_{blob} \sim (5–7) \times 10^{17}$ cm during previous quiescent and flare states of 3C 279 (Paper II). If the X-ray emission does not significantly change between Epochs A and B, then the emitting region size R_b' may decrease as acceleration and emission increase. In all our models the minimum jet opening angle has a reasonable value.

It is clear within our analysis that first- and second-order Fermi accelerations are sufficient to power the observed flare, even assuming that the source particles are from a thermal distribution. Thus, no other forms of acceleration are necessary to explain the behavior. However, we briefly explore reconnection because it is part of the existing conversation in the literature of this particular flare's acceleration. Magnetic reconnection can in principle describe a rapid flare with very short variability timescale and a hard particle spectrum, both of which are observed. It requires a magnetization parameter, $\sigma \gg 1$. This can be constrained by (Paper I)

$$\sigma < \sigma_{max} = \frac{3D_0 R_b'}{c}, \qquad (25)$$

based on the maximum Larmor radius of an electron that fits inside the blob. The model calculations of σ_{max} can be found in Table 2. In all models, $\sigma_{max} \sim 1$. Since particle reconnection generally requires $\sigma \gg 1$, a lack of particle acceleration by reconnection is consistent with our models. First- and second-order Fermi acceleration are sufficient to explain the emission during the epochs explored here.

Equipartition is used in a wide range of astrophysical analyses, and can be used as a simplifying assumption for otherwise poorly constrained parameters (e.g., Dermer et al. 2014). There is an uncertainty involved, since the power in protons (either accelerated or "cold") is poorly constrained from the modeling (e.g., Beck & Krause 2005). In the discussion in the rest of this section, we neglect the presence of protons in the jet; however, this uncertainty should be kept in mind. In our models for 3C 279 we find the power in the field P_B is not always equivalent to the power in the jet electrons P_e, although $P_B \sim P_e$ within an order of magnitude or two for previously examined epochs (Paper II). Our Model A analysis shows the quiescent jet was close to equipartition (Table 2), where the equipartition parameter $\zeta_e \equiv P_e/P_B = 1$ represents an equipartition state. However, in all of the B models $P_B \ll P_e$ (Table 2), and the jet is strongly electron dominated. The larger the frequency integrated flux, the larger the equipartition parameter for Epoch B. This is consistent with the analysis by Hayashida et al. (2015) for the Epoch B flare; they also found the jet was matter dominated. A matter dominant jet might be indicative of a larger than usual influx of electrons into the emitting region. An analysis for Epoch B was attempted, in which $P_B \approx P_e$, but the jet opening angle was unphysically large, and therefore it is not presented here.

Neglecting protons, the total jet power $P_{B+e} = P_e + P_B$. For a maximally rotating BH, one expects that the accretion power $P_a = L_{disk}/0.4$, giving $P_a = 2.4 \times 10^{45}$ ergs^{-1} for our models. For all our models except Model B1, $\mu_a \equiv P_{B+e}/P_a$ is a factor $\sim$ a few (Table 2). This is consistent with extracting spin from a BH with a magnetically arrested accretion disk (Tchekhovskoy

Table 3
Power in the Physical Components

Variable (Unit)	Model A	Model B1	Model B2	Model B3
P'_{esc} (erg s^{-1})	-6.0×10^{31}	-5.3×10^{35}	-9.6×10^{33}	-2.9×10^{33}
P'_{inj} (erg s^{-1})	8.8×10^{29}	1.0×10^{32}	8.6×10^{30}	1.3×10^{31}
P'_{sto} (erg s^{-1})	3.2×10^{43}	1.9×10^{44}	7.2×10^{42}	1.4×10^{42}
$P'_{\mathrm{sh+ad}}$ (erg s^{-1})	-2.4×10^{43}	$+4.7 \times 10^{43}$	-3.6×10^{42}	-1.8×10^{41}
P'_{syn} (erg s^{-1})	-2.4×10^{41}	-6.3×10^{41}	-1.3×10^{40}	-3.0×10^{39}
P'_{EC} (erg s^{-1})	-8.6×10^{41}	-2.4×10^{44}	-3.6×10^{42}	-1.3×10^{42}
%σ_{err}	2.9	0.03	0.03	0.04

et al. 2011). However, for Model B1, $\mu_a = 8.8$, which may be too large too extract from the Blandford & Znajek (1977) process.

The total jet luminosity due to particle radiation (e.g., Finke et al. 2008)

$$L_{\mathrm{jet}} = \frac{2\pi d_L^2}{\Gamma^2} \int_0^\infty \frac{d\epsilon}{\epsilon} \left(f_{\epsilon_{\mathrm{obs}}}^{\mathrm{syn}} + f_{\epsilon_s}^{\mathrm{SSC}} + \sum_{j=1}^J f_{\epsilon_s}^{\mathrm{EC},(j)} \right), \quad (26)$$

is reported in Table 2. The radiative efficiency L_{jet}/P_{B+e} is expected to be <1. This is indeed the case, for all models except for Model B1.

Based on the excessive μ_a and large radiative efficiency ($L_{\mathrm{jet}}/P_{B+e} > 1$), we believe Model B1 is unphysical and cannot explain Epoch B.

The injection luminosity L_{inj} of Epoch A is similar to other injection luminosities we have found for 3C 279 in other epochs (Paper II). The injection luminosities for the B models are somewhat higher due primarily to the increased rate of particle injection. This supports the idea of an influx of particles from the accretion disk area instigating the flare.

3.4. Energy Budget

One benefit of the Fokker–Planck equation (or transport equation) formalism is the conservation of energy. We can compute the rate of energy gains and losses in electrons (in the co-moving frame: that is, injected into the system (P'_{inj}); escaping the system (P'_{esc}); accelerated by the second-order Fermi acceleration process (P'_{sto}); accelerated by first-order Fermi acceleration or lost by adiabatic expansion ($P'_{\mathrm{sh+ad}}$); lost by synchrotron (P'_{syn}) or EC radiation (P'_{EC}). The first-order Fermi acceleration and adiabatic losses are taken together, since in practice separating them introduces an unconstrainable free parameter in our formalism. (See Paper II for the details on how these rates are calculated.)

The component powers resulting from our simulations for the epochs examined here can be found in Table 3. The relative error percentages found by adding up the powers are low (within expected numerical errors), indicating the expected energy balance.

Since in all cases $P'_{\mathrm{sto}} > P'_{\mathrm{sh+ad}}$, the particles are primarily accelerated by the second-order Fermi process, rather than first-order Fermi acceleration. This is consistent with our results for other SEDs in Papers I and II. First-order Fermi acceleration dominates over adiabatic losses for only Model B1, since this is the only simulation where $P'_{\mathrm{sh+ad}} > 1$. This is consistent with this being the only model with $A_{\mathrm{ad+sh}} > 0$ (Table 1). For the other models, adiabatic losses are an important energy loss mechanism. For Model A, adiabatic losses dominate over radiative losses by a factor of ~ 100. For Models B2 and B3,

they are the same order of magnitude as radiative losses. We note the Epoch B models have a much larger $P'_{\mathrm{EC}}/P'_{\mathrm{syn}}$ than the Epoch A simulation, as expected, since Epoch B has a much larger A_C than Epoch A.

The injection energy is not an important contribution to the energy budget. The escape power is always slightly larger in magnitude than the injection power because the escape occurs in the Bohm limit, meaning higher energy particles are preferentially lost from the electron population (Paper I).

3.5. Acceleration Timescales

An additional benefit of the particle transport method we employ is the ability to compare the timescales for each physical process, as expressed by the coefficients in Equations (7)–(10), which have units of [s^{-1}] (Paper I). Of particular interest during the flare is the acceleration timescale, because the flare duration is short (~ 12 hr) and the flux-doubling timescale is rapid (~ 2 hr). Hence the acceleration mechanism providing energy to the flare must act on commensurate timescales (e.g., Hayashida et al. 2015; Paliya et al. 2016).

The mean timescale for the second-order Fermi acceleration of electrons via hard-sphere scattering with magnetohydro-dynamic (MHD) waves is computed in the frame of the observer using

$$t_{\mathrm{sto}} = \frac{1+z}{\delta_D} \frac{1}{4D_0}, \quad (27)$$

where the factor of 4 comes from the derivative separating the broadening and drift coefficient components of the second-order Fermi up-scattering. First-order Fermi acceleration is closely linked with adiabatic expansion in the transport model during analysis of the SED, since both processes have the same energy dependence (Paper I). However, we constrain the first-order Fermi acceleration timescale by assuming that the energy loss rate due to adiabatic expansion during the flare, $A_{\mathrm{ad}}^{\mathrm{flare}}$, is the same as during quiescence, $A_{\mathrm{ad}}^{\mathrm{quiescent}}$. Thus, the first-order Fermi acceleration timescale during the flare can be constrained using Model A as the limiting case, which yields

$$t_{\mathrm{sh}} \lesssim \frac{1+z}{\delta_D} \frac{1}{A_{\mathrm{ad+sh}}^{\mathrm{flare}} - A_{\mathrm{ad}}^{\mathrm{quiescent}}}, \quad (28)$$

where $A_{\mathrm{ad}}^{\mathrm{quiescent}} \lesssim A_{\mathrm{sh+ad}}^{\mathrm{quiescent}}$ (values in Table 1). The total acceleration timescale, t_{acc}, depends on both the first- and second-order Fermi timescales, t_{sh} and t_{sto}, respectively, via

$$t_{\mathrm{acc}} = \frac{1}{t_{\mathrm{sh}}^{-1} + t_{\mathrm{sto}}^{-1}}, \quad (29)$$

Table 4
Simulated Emission and Acceleration Timescales

Variable (Unit)	Model A	Model B1	Model B2	Model B3
$t_{\rm sto}$ (hr)	0.7	2.5	0.2	0.1
$t_{\rm sho}$ (hr)	⋯	$\lesssim 1.1$	$\lesssim 3.5$	$\lesssim 0.5$
$t_{\rm acc}$ (hr)	$\leqslant 0.7$	$\lesssim 0.7$	$\lesssim 0.2$	$\lesssim 0.1$

where the value of $t_{\rm sh}$ is an upper limit given by Equation (28). The values provided in Table 4 for $t_{\rm acc}$ are therefore also upper limits. Thus, first- and second-order Fermi acceleration rates, as included in the model, are sufficiently rapid to produce the observed flux-doubling timescale for the 2013 flare.

4. Discussion

In the following section, we discuss the physical implications of the analysis, compare our results with previous literature, and summarize our primary findings.

4.1. Physical Interpretations

Blazar jets are thought to contain standing shocks (e.g., Marscher et al. 2008). A superluminal blob passing through a standing shock will increase the amount of first-order Fermi acceleration (e.g., Marscher 2012), which is consistent with the Epoch B models, compared with our model for Epoch A (Table 1). MHD simulations demonstrate that first-order Fermi acceleration gives rise to higher levels of stochastic turbulence downstream of the shock (e.g., Inoue et al. 2011), which agrees with the increase in second-order Fermi acceleration during the flare analyses (Table 1). Both the first- and second-order Fermi acceleration contribute to the higher maximum electron Lorentz factor as well as the higher number of high-energy particles (see Figure 4). These are important to the higher frequency position of each emission component in the SED.

As particle energy increases, so does the Larmor radius ($r_{\rm L} = \gamma m_e c^2 q^{-1} B^{-1}$). A particle with a larger Larmor radius, will travel preferentially closer to the edge or sheath of the jet (e.g., Hillas 1984). If the magnetic field is radially dependent (stronger near the jet core), then the apparent magnetic field of the jet may be lower by a factor of a few when more particles spend more time near the edge of the emitting region in the jet. Massaro et al. (2004) discuss a log-parabolic particle distribution (which can be formed by second-order Fermi acceleration; Tramacere et al. 2011) as one in which the confinement efficiency of a collimating magnetic field decreases with increasing gyro-radius. This physical interpretation can explain the smaller magnetic field (Table 1) and the greater loss to escaping particles (Table 3), during the flare.

In Model B1, the first-order Fermi acceleration contributes more than in Models B2 and B3. This is consistent with the smaller bulk Lorentz factor (recall we assume $\delta_{\rm D} = \Gamma$, Table 1), since increased first-order Fermi acceleration indicates a given particle is scattered through the shock front more times. Thus, even larger Larmor radii may indicate that emitting particles occupy some of the jet sheath, where the magnetic field is significantly lower, which explains the 95% drop in field strength in the analysis of the flare (Table 1). While the interpretation is somewhat more extreme for Model B1, the second-order Fermi acceleration coefficient and variability timescale are more similar to Model A than are Models B2 and B3. However, Model B1 has an unphysical

radiative efficiency (Table 2), suggesting that the simulation of extreme SSC emission employed therein is not an appropriate representation of the data.

Models B2 and B3 are also well described by a large influx of material injected into the base of the jet, which may strengthen the effects of particle acceleration at a shock while temporarily weakening the comparative power of the magnetic field, without initiating widespread reconnection. It would be particularly interesting to study high-energy polarization in blazar flares, especially as several new instruments are in the planning stages. X-ray and γ-ray polarimetry can more definitively separate leptonic from hadronic models, elucidate the shock versus magnetic reconnection debate, and provide a new avenue through which to explore the geometry of the acceleration/emission region (e.g., Dreyer & Böttcher 2019).

4.2. Comparison with Previous Work

Besides reporting on the 2013 December epochs that we model here (and other epochs that we do not consider), Hayashida et al. (2015) also modeled these epochs with the BLAZAR code (Moderski et al. 2003). They used a double broken power-law ED to model Epoch A, and a broken power-law distribution to model Epoch B. Similar to our modeling, Hayashida et al. (2015) found that EC/dust dominated the γ-ray emission during Epoch A and EC-BLR dominated during Epoch B. For Epoch A, they found a larger magnetic field, lower Γ, and larger $r_{\rm blob}$. They modeled Epoch B with two sets of parameters. Their model parameters for this epoch are generally similar to ours for our Models B2 and B3, although or magnetic field for our Model B1 is quite lower compared to their models. Our models for Epoch B have similar $r_{\rm blob}$, but larger Γ for our Models B2 and B3.

Asano & Hayashida (2015) model the 2013 December flare with a time-dependent model (Asano et al. 2014) that treats particle acceleration quite similar to ours. They model both the SED and the γ-ray light curve. In their model, scattering of a UV field (presumably representing a BLR) dominates the γ-ray emission and they have $\Gamma = 15$ and $r_{\rm blob} \sim 6 \times 10^{16}$ cm, so their emitting region is closer to the BH than in our models (to a degree consistent with our use of a stratified BLR, Paper II). Their model successfully reproduces the observed LAT γ-ray light curve, although the high Γ may be a problem for models of jet acceleration by magnetic dissipation.

The 2013 flare was further examined by Paliya et al. (2016) using time-dependent lepto-hadronic and two-zone leptonic models. Those authors examined a 3 day window that included the flare, and noted a 3 hr flux-doubling timescale. They adopted a smooth broken power law as the particle distribution, and found that the isolated flare could represent γ-ray emission from a smaller blob, while the rest of the spectrum was produced in a larger volume. Another possibility is that proton acceleration could power the enhanced γ-ray emission. The inclusion of significant non-flare data in the analysis of Paliya et al. (2016) raises concerns about identifying the physics of the flare specifically. Hence the shape of the ED and the nature of the associated particle acceleration mechanism(s) during the 2013 flare from 3C 279 are still open questions.

4.3. Summary

Our model from Paper II included a numerical steady-state solution to a particle transport equation that included first- and

second-order Fermi acceleration and particle escape. Particles in this single homogeneous blob can lose energy to adiabatic expansion, synchrotron radiation, and inverse-Compton scattering of incident photon fields, including SSC, EC/disk, EC/dust, and EC/BLR, where the BLR is composed of 26 individual lines radiating at infinitesimally thin concentric shells. We added to this $\gamma\gamma$-absorption due to the accretion disk, dust torus, and stratified BLR consistent with the emission and Compton scattering geometry (Finke 2016). We applied our model to the SED of the extremely Compton-dominant flare of 3C 279 observed on 2013 December 20 (Hayashida et al. 2015). The preceding 3 days of quiescent data are similarly analyzed as a baseline for the flare simulations. We derive a simplified version of the Thomson regime approximation (Paper I), which assists in the interpretation of the ED. Our primary results are as follows:

1. It is possible to simulate the acceleration in the flare SED with reasonable levels of only first- and second-order Fermi processes (with the latter process dominating in our models). Acceleration by reconnection is not needed, and the maximum magnetization parameter (σ) found from our model parameters is consistent with this.
2. It is possible for the BLR to be the dominant EC component without significant $\gamma\gamma$ absorption from BLR photons.
3. The quiescent period displays electron and field powers near equipartition, while the flare is strongly electron dominated.
4. There is insufficient energy available for the X-rays to have undergone a flare comparable to the γ-ray flare simultaneously.
5. The simplified ED analysis clarifies that first- and second-order Fermi acceleration can influence different components of the overall ED.
6. Based on our modeling of Epoch B, the νF_ν flux at ≈ 10 MeV is likely $<10^{-9}$ ergs^{-1} cm^{-2} (i.e., Model B1 is highly unlikely). The emission in this energy range could be probed by a future γ-ray mission such as e-Astrogam or the All-sky Medium Energy Gamma-ray Observatory (AMEGO), which could provide further constraints on blazar SEDs.

This model has been informative in the analysis of this particularly unusual flare. We plan to use the same model to analyze other intriguing blazar behaviors. Additionally the simplified analytic ED can be applied to astrophysical jets more broadly, where both first- and second-order Fermi acceleration are expected to contribute.

Appendix A
Derivation of the Thomson ED Features

In Paper I, the electron transport equation is solved analytically in the Thomson limit. That steady-state analytic solution (Equation (11))

$$
N_e(\gamma) = \frac{\dot{N}_{\rm inj} e^{b\gamma_{\rm inj}/2}}{b D_0 \gamma_{\rm inj}^{2+(a/2)}} \frac{\Gamma[\mu - \kappa + 1/2]}{\Gamma[1 + 2\mu]}
$$
$$
\times\, e^{-b\gamma/2} \gamma^{a/2} \begin{cases} \mathcal{M}_{\kappa,\mu}(b\gamma)\mathcal{W}_{\kappa,\mu}(b\gamma_{\rm inj}), & \gamma \leqslant \gamma_{\rm inj} \\ \mathcal{M}_{\kappa,\mu}(b\gamma_{\rm inj})\mathcal{W}_{\kappa,\mu}(b\gamma), & \gamma \geqslant \gamma_{\rm inj} \end{cases}, \quad (30)
$$

introduces the idea that the ED shape can be interpreted physically if it comes from first principles. In this appendix, that solution is simplified by making some mathematical approximations for the phase spaces applicable to the physical regimes of interest for blazars. The simplified functions provided, may provide insight into a broader range of blazar activity in consistent parameter spaces, as well as any astrophysical jet for which the same assumptions are valid.

The ED as stated in Equation (11) for the steady-state solution is branched, with continuity enforced at the injection energy. The derivation begins with the branch above the injection energy, $\gamma_{\rm inj} < \gamma$

$$
N(\gamma) = \frac{\dot{N}_{\rm inj}}{D_0} b^{-1} \gamma^{a/2} \gamma_{\rm inj}^{-(a/2)-2} \exp\left[\frac{b\gamma_{\rm inj}}{2}\right]
$$
$$
\times \exp\left[-\frac{b\gamma}{2}\right] \frac{\Gamma[1/2 + \mu - \kappa]}{\Gamma[1 + 2\mu]} \mathcal{M}_{\kappa,\mu}(b\gamma_{\rm inj})\mathcal{W}_{\kappa,\mu}(b\gamma),
$$
$$
(31)
$$

because the injection energy is almost always smaller than the energies of interest in the rest of the ED, since the injection energy originates from a thermal distribution before arriving in the emitting blob.

The Whittaker functions are replaced with their confluent hypergeometric counterparts

$$
N(\gamma) = \frac{\dot{N}_{\rm inj}}{D_0} b^{-1} \gamma^{a/2} \gamma_{\rm inj}^{-(a/2)-2} \exp\left[\frac{b\gamma_{\rm inj}}{2}\right]
$$
$$
\times \exp\left[-\frac{b\gamma}{2}\right] \frac{\Gamma[1/2 + \mu - \kappa]}{\Gamma[1 + 2\mu]}
$$
$$
\times \exp\left[\frac{-b\gamma_{\rm inj}}{2}\right] b^{(1/2)+\mu} \gamma_{\rm inj}^{(1/2)+\mu}
$$
$$
\times M[1/2 + \mu - \kappa, 1 + 2\mu, b\gamma_{\rm inj}]
$$
$$
\times \exp\left[\frac{-b\gamma}{2}\right] b^{(1/2)+\mu} \gamma^{(1/2)+\mu}
$$
$$
\times U[1/2 + \mu - \kappa, 1 + 2\mu, b\gamma], \quad (32)
$$

(Slater 1960), and the electron number distribution is simplified,

$$
N(\gamma) = \frac{\dot{N}_{\rm inj}}{D_0} b^{a+3} \gamma^{a+2} \exp[-b\gamma] \frac{\Gamma[1/(b\tau)]}{\Gamma[a+4]}
$$
$$
M[1/(b\tau), a+4, b\gamma_{\rm inj}] U[1/(b\tau), a+4, b\gamma],
$$
$$
(33)
$$

where the Whittaker coefficients are

$$
\kappa = 2 - \frac{1}{b\tau} + \frac{a}{2}, \quad \text{and} \quad \mu = \frac{a+3}{2}, \quad (34)
$$

as stated after Equation (11).

The exact expression for the confluent hypergeometric U-function is given by

$$U[\hat{a}, \hat{b}, \hat{x}]$$
$$= \frac{\pi}{\sin[\pi\hat{b}]}\left(\frac{M[\hat{a}, \hat{b}, \hat{x}]}{\Gamma[1 + \hat{a} - \hat{b}]\Gamma[\hat{b}]} - \frac{\hat{x}^{1-\hat{b}}M[\hat{a}, \hat{b}, \hat{x}]}{\Gamma[\hat{a}]\Gamma[2 - \hat{b}]}\right), \quad (35)$$

(Slater 1960; Abramowitz & Stegun 1972), which is undefined for nonpositive integer inputs to the Γ-functions.

In comparing the model with blazar SED data, the combined emission coefficient is small ($b \sim 10^{-6}$), which makes the final argument in the confluent hypergeometric functions small at most Lorentz factors for which there is a meaningful number of electrons ($\gamma_{\max} \lesssim b^{-1}$). When $b\gamma \ll 1$ is assumed, the confluent hypergeometric M-function can be approximated as

$$M[\hat{a}, \hat{b}, \hat{x} \to 0] = 1 \quad (36)$$

(Slater 1960; Abramowitz & Stegun 1972). Thus, the electron number distribution can be expressed as

$$N(\gamma) = \frac{\dot{N}_{\mathrm{inj}}}{D_0}b^{2\mu}\gamma^{a+2}\exp[-b\gamma]$$
$$\times \left(\frac{\pi}{\sin[\pi(a+4)]}\frac{\Gamma[(b\tau)^{-1}]}{\Gamma^2[a+4]\Gamma[(b\tau)^{-1} - a - 3]}\right.$$
$$\left. - \frac{\pi}{\sin[\pi(a+4)]}\frac{(b\gamma)^{-a-3}}{\Gamma[a+4]\Gamma[-a-2]}\right), \quad (37)$$

with appropriate substitutions, and incomplete factoring which becomes convenient. It will also become convenient to name the first term on the right-hand side of the equation (RHS-1) and the second term on the right-hand side of the equation (RHS-2).

Both terms (RHS-1 and RHS-2) can be simplified, using combinations of the reflection and recursion relations for Γ-functions,

$$\Gamma[z]\Gamma[1 - z] = \frac{\pi}{\sin[\pi z]}, \quad (38)$$

and

$$\Gamma[z + 1] = z\Gamma[z], \quad (39)$$

respectively (Abramowitz & Stegun 1972).

Applying Equations (38) and (39) to the ED in Equation (37), the solution is simplified to

$$N(\gamma) = \frac{\dot{N}_{\mathrm{inj}}}{D_0}\gamma^{-1}\exp[-b\gamma]$$
$$\times \left(\frac{(b\gamma)^{a+3}\Gamma[(b\tau)^{-1}]\Gamma[-a-3]}{\Gamma[a+4]\Gamma[(b\tau)^{-1} - a - 3]} + \frac{1}{3+a}\right). \quad (40)$$

In each blazar and epoch examined in this work and previous analyses (Papers I and II) the Bohm timescale $\tau \gg b^{-1}$. It follows that $(b\tau)^{-1} \ll |a + 3|$, and adopting this approximation, the Γ-functions can be simplified as

$$\Gamma[(b\tau)^{-1} - a - 3] \approx \Gamma[-a - 3] \quad \text{and}$$
$$\Gamma[(b\tau)^{-1}] \approx b\tau, \quad (41)$$
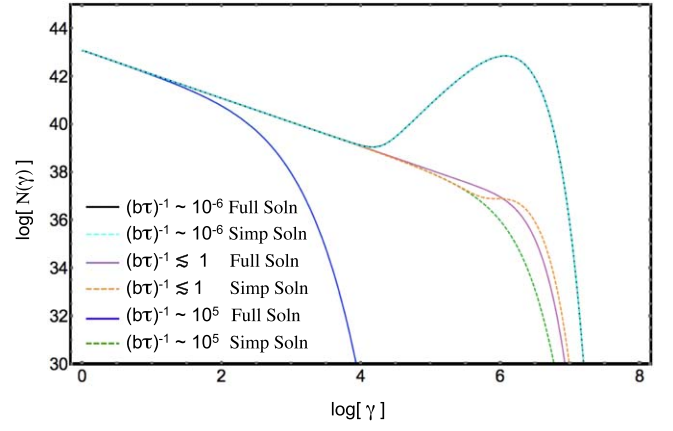
Figure 6. Simplified ED (Equation (42)) is more sensitive to the limit of $(b\ \tau)^{-1} \ll 1$ than to $b\gamma \ll 1$, when compared with the full Thomson ED (Equation (31)) in the $\gamma_{\mathrm{inj}} < \gamma$ regime.

since $\Gamma^{-1}[z] = z + \mathcal{O}(z^2)$ for $z \ll 1$ (Abramowitz & Stegun 1972). Applying the approximation in Equation (41) to the ED in Equation (40) gives

$$N(\gamma) = \frac{\dot{N}_{\mathrm{inj}}}{D_0}\exp[-b\gamma]\left(\frac{\tau b^{a+4}\gamma^{a+2}}{\Gamma[a+4]} + \frac{\gamma^{-1}}{3+a}\right). \quad (42)$$

This equation was tested for a range of parameter values, and found to agree completely with the analytic solution for parameters consistent with the stated assumptions, namely, $\gamma > \gamma_{\mathrm{inj}}$, $b\gamma \ll 1$ and $(b\tau)^{-1} \ll 1$.

Figure 6 explores the precision of the approximations in the simplified analytic ED (Equation (42)) in comparison to the full analytic Thomson ED (Equation (31)) for $\gamma_{\mathrm{inj}} < \gamma$. The parameters used in this example are similar to those from Model B1 (Table 1), however that model formally included the Klein–Nishina cross section. Mathematically, we assume that $b\gamma \ll 1$ in order to use the approximation in Equation (36), however at $\gamma \sim 10^7$, $b\gamma \sim 25$ for the case where $(b\tau)^{-1} \ll 1$ (black and cyan), and there is no discernible difference between the simplified and Thomson solutions. Attempts at increasing the value of b, generally resulted in both solutions experiencing exponential drops at a comparably smaller Lorentz factor γ. Thus, the approximation is fairly robust. Conversely, Figure 6 demonstrates that the simplified ED is more sensitive to the limit $(b\tau)^{-1} \ll 1$ required for Equation (41). When the limit is satisfied, the simplified and Thomson solutions are in agreement (black and cyan), and where $(b\tau)^{-1} \gg 1$, the solutions diverge. In the case of $(b\tau)^{-1} \lesssim 1$, the simplified solution is visibly different, but perhaps sufficient for some applications.

Equation (42) is shown in Figure 7 for a sample set of parameters that illustrate the features well, and wherein only the first-order Fermi/adiabatic parameter a is varied, while all other parameters are fixed. The high-energy turnover in the ED is controlled by the leading exponential $e^{-b\gamma}$. RHS-1 from Equation (42) can be the dominant term throughout, especially for more negative values of a in this example, but also depending on b and D_0 more generally. For less negative (or increasingly positive) values of a, sometimes, RHS-2 becomes the dominant term at low energies, depending on the relative magnitude of each power law. RHS-2 is defined by a γ^{-1} power law in all cases, until the exponential turnover. RHS-1 is
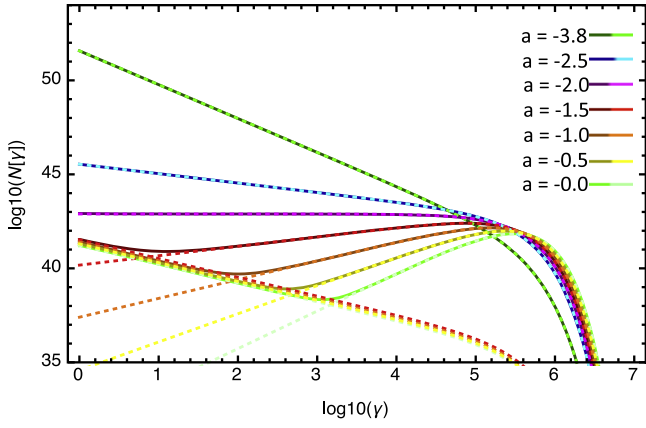
Figure 7. ED for changing a values, where the dotted lines are the separate terms in Equation (42). The dotted curves for RHS-1 are those which dominate the ED at higher energies, while the dotted curves for RHS-2 are shown in the same color scheme. The dotted curves for RHS-2 are only shown if they have a region of dominance (at lower energies) in the overall ED; otherwise they were suppressed for clarity because they crowded the existing RHS-2 curves.
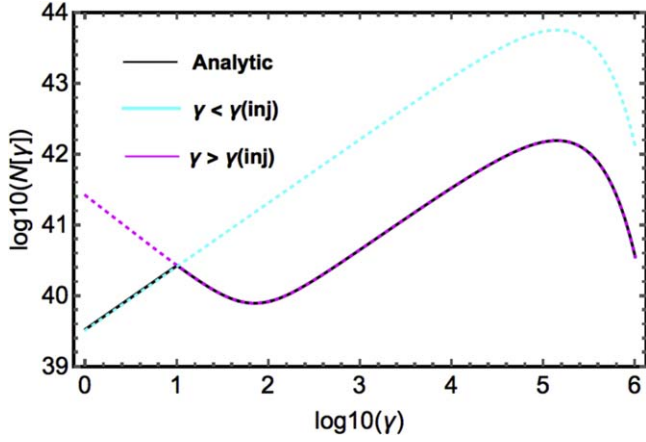
Figure 8. ED for $a = -1$, where we let $\gamma_{\rm inj} = 10$ in order to observe the injection energy cusp. The underlying black line is the full analytic ED shown in Equation (11) of Section 2 (Paper I). The magenta dotted line is the solution from Equation (42) for $\gamma \geqslant \gamma_{\rm inj}$, while the cyan line is the solution in Equation (44) for $\gamma \leqslant \gamma_{\rm inj}$.

defined by a γ^{a+2} power law, which is why the lower energy slope of this curve changes with a, and always produces a horizontal feature for $a = -2$, regardless of the other parameters.

In this paper, we argue against using substantial injection energies. Thus, all of our EDs are essentially calculated for $\gamma \geqslant \gamma_{\rm inj}$. However, the original steady-state analytic solution (Paper I) did not carry that constraint. So, for completeness, in the case where $\gamma \leqslant \gamma_{\rm inj}$, the ED is given by

$$
N(\gamma) = \frac{\dot{N}_{\rm inj}}{D_0} b^{-1} \gamma^{a/2} \gamma_{\rm inj}^{-(a/2)-2} \exp\left[\frac{b\gamma_{\rm inj}}{2}\right]
$$
$$
\times \exp\left[-\frac{b\gamma}{2}\right] \frac{\Gamma[1/2 + \mu - \kappa]}{\Gamma[1 + 2\mu]} \mathcal{M}_{\kappa,\mu}(b\gamma) \mathcal{W}_{\kappa,\mu}(b\gamma_{\rm inj}).
$$
(43)

Following the same arguments presented above, the ED can be simplified to

$$
N(\gamma) = \frac{\dot{N}_{\rm inj}}{D_0} \exp[-b\gamma] \left(\frac{\tau b^{a+4} \gamma^{a+2}}{\Gamma[a+4]} + \frac{\gamma_{\rm inj}^{-a-3} \gamma^{a+2}}{3+a} \right). \quad (44)
$$

In this approximate ED, RHS-1 is identical to RHS-1 in Equation (42), and essentially makes no contribution. In Equation (44), RHS-2 normalizes the ED to the appropriate magnitude for the injection energy, and γ^{a+2} still governs the shape.

For physical SED evaluations, the analysis tends to concentrate in the regions of parameter space where RHS-1 in Equation (42) dominates. This expression could be helpful to those who assume a power-law ED with an exponential cutoff, since it provides a physical interpretation behind that general shape, including first-order Fermi and diffusive acceleration, as well as synchrotron and Thomson emission. However the analysis of Epoch B demonstrates the usefulness of the full simplified solution in Equation (42) for a variety of ED shapes.

To further expound upon Equation (42), the leading factor $e^{-b\gamma}$ provides a turnover in the ED at high energies, which is dependent upon the nonthermal cooling coefficients for synchrotron radiation and Compton scattering. Note the first term on the right-hand side of Equation (42), where $N(\gamma) \propto \gamma^{a+2}$ implies that where this term dominates, the lower energy slope is defined by $(a + 2)$, where the first-order Fermi acceleration/adiabatic expansion coefficient a is often negative in blazar spectral analysis (Papers I and II), and will always be flat for $a = -2$.

There are parameter regimes, especially in the samples provided in Figure 8, where $a > -2$, and it is possible to see the second term in Equation (42) become dominant in the lower energy domain (but still above the injection energy). In this scenario, the change occurs where the two terms in Equation (42) become equivalent, or at the Lorentz factor

$$
\gamma = \gamma_{\rm dip} = \frac{1}{b} \left(\frac{\Gamma[a+3]}{b\tau} \right)^{1/(a+3)}, \quad (45)
$$

as is the case for the Epoch B analysis in Section 3.

For $\gamma_{\rm inj} < \gamma < \gamma_{\rm dip}$, if RHS-2 dominates in Equation (42), then the electron population is dominated by diffusion from the injection energy. The steady-state solution contains a continuous, monochromatic particle injection, and the transport equation allows the electron population to evolve over time, where the steady-state is an equilibrium snapshot. The second term (RHS-2) electrons are those that did not have time to get sufficiently caught up in the acceleration processes to lose the signature of their initial injection.

For $\gamma_{\rm dip} < \gamma < 1/b_{\rm tot}$, RHS-1 of Equation (42) tends to dominate. In this domain, acceleration and diffusion processes are in perfect balance with one another, and there is no net transport. However, it is possible for the "acceleration" portion to be negative due to adiabatic expansion, hence electrons are "accelerated" to lower energies. When acceleration a is stronger (more positive), $\gamma_{\rm dip}$ is pushed to higher energies, as the electrons form an increasingly bimodal distribution (see Figure 8).

12

Appendix B
Acceleration Term Dependences in the Simplified Solution

The electron number distribution is defined according to the distribution function (Paper I)

$$N = 4\pi (m_e c)^3 \gamma^2 f(\gamma) \tag{46}$$

for the steady-state case. Consider the domain of the simplified ED, where $\gamma > \gamma_{\rm dip} > \gamma_{\rm inj}$ (Equation (42))

$$N \propto \gamma^{a+2}. \tag{47}$$

It follows that the distribution function follows the proportionality

$$f \propto \gamma^a, \text{ or } \quad f(\gamma) = A_* \gamma^a, \tag{48}$$

where A_* is a place-holding constant. The particle flux due to stochastic diffusion (a second-order process; Equation (59) of Paper I)

$$\dot{N}_{\rm sto} = -a D_0 A_* \gamma^{a+3}, \tag{49}$$

and the particle flux due to first-order Fermi acceleration (including adiabatic expansion)

$$\dot{N}_{\rm ad+sh} = A_{\rm ad+sh} \gamma^3 f = A_{\rm ad+sh} A_* \gamma^{a+3} \tag{50}$$

can be combined into the particle flux due to the sum of first- and second-order Fermi acceleration

$$\dot{N}_{\rm sum} = \dot{N}_{\rm sto} + \dot{N}_{\rm ad+sh} = -a D_0 A_* \gamma^{a+3} + A_{\rm ad+sh} A_* \gamma^{a+3} \equiv 0, \tag{51}$$

since $A_{\rm ad+sh} \equiv a D_0$, demonstrating that these processes perfectly balance in all cases for RHS-1 of Equation (42).

There are blazar data analyses where the first-order Fermi coefficient is $a < -2$, and it is possible to see the second term in Equation (42) become dominant in the lower energy domain (but still above the injection energy). In this scenario, the change occurs where the two terms become equivalent

$$\frac{b^{a+3} \gamma^{a+2} \Gamma(1/(b\tau))}{\Gamma(a+4)} = \frac{1}{\gamma(a+3)}, \tag{52}$$

which can be solved for the Lorentz factor where the two terms cross,

$$\gamma = \gamma_{\rm dip} = \left[\frac{1}{(a+3)b^{a+3}} \frac{\Gamma(a+4)}{\Gamma(1/(b\tau))} \right]^{1/(a+3)}. \tag{53}$$

For $\gamma_{\rm inj} < \gamma < \gamma_{\rm dip}$, if the second term dominates, then the electron population is dominated by diffusion from the injection energy. The continuous particle injection to the transport equation allows the electron population to evolve over time, where the steady-state is an equilibrium snapshot. The second term represents electrons that did not have time to get sufficiently caught up in the first-order Fermi acceleration processes to lose the signature of their initial injection.

The ED where RHS-2 of Equation (42) dominates is described by the proportion

$$N(\gamma) \propto \frac{1}{\gamma}, \tag{54}$$

meaning that the distribution function is given by (Paper I)

$$f(\gamma) \propto \frac{N}{\gamma^2} \quad \text{or} \quad f(\gamma) = \frac{A_*}{\gamma^3}. \tag{55}$$

The particle flux due to second-order Fermi diffusion is given by (Equation (59) of Paper I)

$$\dot{N}_{\rm sto} = -D_0 \gamma^4 \frac{\partial f}{\partial \gamma} = 3 D_0 A_*, \tag{56}$$

and the particle flux due to first-order Fermi acceleration (including adiabatic expansion) is

$$\dot{N}_{\rm ad+sh} = A_{\rm ad+sh} \gamma^3 f = A_{\rm ad+sh} A_*. \tag{57}$$

The rates of first- and second-order Fermi acceleration can be combined into the total rate

$$\dot{N}_{\rm sum} = \dot{N}_{\rm sto} + \dot{N}_{\rm ad+sh} = A_* D_0 (3 + a), \tag{58}$$

where the first-order Fermi acceleration and second-order Fermi diffusion processes are not perfectly balanced for all parameters, but can balance where $a = -3$. As it happens, this is similar to first-order Fermi acceleration/adiabatic expansion parameters we find when comparing to data. Specifically, $a \sim -3.8 \pm 0.3$ (Paper II), indicating that both parameters are necessary.

For $\gamma_{\rm dip} < \gamma < 1/b$, the first term tends to dominate. In this regime, first-order Fermi (with adiabatic expansion) and second-order Fermi acceleration processes are in perfect balance with one another, and there is no net transport. However, it is possible for the first-order "acceleration" portion to be negative due to adiabatic expansion, hence electrons are "accelerated" to lower energies. When first-order Fermi acceleration $A_{\rm ad+sh}$ is stronger (more positive), $\gamma_{\rm dip}$ is pushed to higher energies, as the electrons form an increasingly bimodal distribution.

It is important to note that while one term may be negligible for specific parameter ranges where another is clearly dominant, no term alone represents a complete, independent solution to the electron transport equation. Therefore, interpretations of the ED must be mindful that the solution terms are not completely separable to maintain a self-consistent picture in the original sense of the transport equation. Recall that we have made a number of assumptions about the ranges of several parameters in order to provide these simplified expressions and their corresponding interpretations. We anticipate that the simplified function forms will be useful, but we encourage some caution in their application.

ORCID iDs

Tiffany R. Lewis https://orcid.org/0000-0002-9854-1432
Justin D. Finke https://orcid.org/0000-0001-5941-7933
Peter A. Becker https://orcid.org/0000-0002-3718-1293

References

Abramowitz, M., & Stegun, I. 1972, Handbook of Mathematical Functions (New York: Dover)
Ackermann, M., Anantua, R., Asano, K., et al. 2016, ApJL, 824, L20
Aharonian, F. A. 2000, NA, 5, 377
Asano, K., & Hayashida, M. 2015, ApJL, 808, L18
Asano, K., Takahara, F., Kusunose, M., Toma, K., & Kakuwa, J. 2014, ApJ, 780, 64
Baring, M. G., Böttcher, M., & Summerlin, E. J. 2017, MNRAS, 464, 4875

Beck, R., & Krause, M. 2005, AN, 326, 414
Bednarek, W., & Protheroe, R. J. 1997, MNRAS, 292, 646
Bednarek, W., & Protheroe, R. J. 1999, MNRAS, 310, 577
Blandford, R. D., & Königl, A. 1979, ApJ, 232, 34
Blandford, R. D., & Levinson, A. 1995, ApJ, 441, 79
Blandford, R. D., & Znajek, R. L. 1977, MNRAS, 179, 433
Błażejowski, M., Sikora, M., Moderski, R., & Madejski, G. M. 2000, ApJ, 545, 107
Blumenthal, G. R., & Gould, R. J. 1970, RvMP, 42, 237
Böttcher, M., Mause, H., & Schlickeiser, R. 1997, A&A, 324, 395
Böttcher, M., Reimer, A., Sweeney, K., & Prakash, A. 2013, ApJ, 768, 54
Chatterjee, R., Jorstad, S. G., Marscher, A. P., et al. 2008, ApJ, 689, 79
Crusius, A., & Schlickeiser, R. 1986, A&A, 164, L16
Dermer, C. D., Cerruti, M., Lott, B., Boisson, C., & Zech, A. 2014, ApJ, 782, 82
Dermer, C. D., Finke, J. D., Krug, H., & Böttcher, M. 2009, ApJ, 692, 32
Dermer, C. D., & Schlickeiser, R. 1993, ApJ, 416, 458
Dermer, C. D., Schlickeiser, R., & Mastichiadis, A. 1992, A&A, 256, L27
Dondi, L., & Ghisellini, G. 1995, MNRAS, 273, 583
Dreyer, L., & Böttcher, M. 2019, in PoS, High Energy Astrophysics in Southern Africa (HEASA2018), 25
Fermi, E. 1949, PhRv, 75, 1169
Finke, J. D. 2016, ApJ, 830, 94
Finke, J. D. 2019, ApJ, 870, 28
Finke, J. D., & Becker, P. A. 2014, ApJ, 791, 21
Finke, J. D., & Becker, P. A. 2015, ApJ, 809, 85
Finke, J. D., Dermer, C. D., & Böttcher, M. 2008, ApJ, 686, 181
Georganopoulos, M., Kirk, J. G., & Mastichiadis, A. 2001, ApJ, 561, 111
Ghisellini, G., & Madau, P. 1996, MNRAS, 280, 67
Grandi, P., Urry, C. M., Maraschi, L., et al. 1996, ApJ, 459, 73
Hayashida, M., Madejski, G. M., Nalewajko, K., et al. 2012, ApJ, 754, 114
Hayashida, M., Nalewajko, K., Madejski, G. M., et al. 2015, ApJ, 807, 79
Hillas, A. M. 1984, ARA&A, 22, 425
Inoue, T., Asano, K., & Ioka, K. 2011, ApJ, 734, 77
Jones, F. C. 1968, PhRv, 167, 1159
Kataoka, J., Mattox, J. R., Quinn, J., et al. 1999, ApJ, 514, 138
Kaur, N., & Baliyan, K. S. 2018, A&A, 617, A59
Kollatschny, W. 2003, A&A, 407, 461
Königl, A. 1981, ApJ, 243, 700
Lewis, T. R., Becker, P. A., & Finke, J. D. 2016, ApJ, 824, 108
Lewis, T. R., Finke, J. D., & Becker, P. A. 2018, ApJ, 853, 6
Liodakis, I., Romani, R. W., Filippenko, A. V., et al. 2018, MNRAS, 480, 5517
MacDonald, N. R., Jorstad, S. G., & Marscher, A. P. 2017, ApJ, 850, 87
Madejski, G., & Sikora, M. 2016, ARA&A, 54, 725
Mannheim, K., & Biermann, P. L. 1992, A&A, 253, L21
Marscher, A. P. 2012, IJMPS, 8, 151
Marscher, A. P., Jorstad, S. G., D'Arcangelo, F. D., et al. 2008, Natur, 452, 966
Massaro, E., Perri, M., Giommi, P., & Nesci, R. 2004, A&A, 413, 489
Moderski, R., Sikora, M., & Błażejowski, M. 2003, A&A, 406, 855
Mücke, A., Protheroe, R. J., Engel, R., Rachen, J. P., & Stanev, T. 2003, APh, 18, 593
Nenkova, M., Sirocky, M. M., Nikutta, R., Ivezić, Ž., & Elitzur, M. 2008, ApJ, 685, 160
Osterman Meyer, A., Miller, H. R., Marshall, K., et al. 2009, AJ, 138, 1902
Paliya, V. S., Diltz, C., Böttcher, M., Stalin, C. S., & Buckley, D. 2016, ApJ, 817, 61
Park, B. T., & Petrosian, V. 1995, ApJ, 446, 699
Peterson, B. M., Grier, C. J., Horne, K., et al. 2014, ApJ, 795, 149
Peterson, B. M., & Wandel, A. 1999, ApJL, 521, L95
Petropoulou, M., & Dermer, C. D. 2016, ApJL, 825, L11
Protheroe, R. J. 1995, NuPhS, 43, 229
Reimer, A., Protheroe, R. J., & Donea, A.-C. 2004, A&A, 419, 89
Romero, G. E., Boettcher, M., Markoff, S., & Tavecchio, F. 2017, SSRv, 207, 5
Shakura, N. I., & Sunyaev, R. A. 1973, A&A, 24, 337
Sikora, M., Begelman, M. C., & Rees, M. J. 1994, ApJ, 421, 153
Sikora, M., Kirk, J. G., Begelman, M. C., & Schneider, P. 1987, ApJL, 320, L81
Slater, L. 1960, Confluent Hypergeometric Functions (Cambridge: Cambridge Univ. Press)
Summerlin, E. J., & Baring, M. G. 2012, ApJ, 745, 63
Tavecchio, F., Maraschi, L., & Ghisellini, G. 1998, ApJ, 509, 608
Tchekhovskoy, A., Narayan, R., & McKinney, J. C. 2011, MNRAS, 418, L79
Tramacere, A., Massaro, E., & Taylor, A. M. 2011, ApJ, 739, 66
Vanden Berk, D. E., Richards, G. T., Bauer, A., et al. 2001, AJ, 122, 549
Vittorini, V., Tavani, M., Cavaliere, A., Striani, E., & Vercellone, S. 2014, ApJ, 793, 98
Wehrle, A. E., Pian, E., Urry, C. M., et al. 1998, ApJ, 497, 178
Zdziarski, A. A., Sikora, M., Pjanka, P., & Tchekhovskoy, A. 2015, MNRAS, 451, 927